npj | Quantum Materials

www.nature.com/npjquantmats

ARTICLE OPEN

Visualizing the evolution from Mott insulator to Anderson insulator in Ti-doped 1*T*-TaS_2

Wenhao Zhang[1,8], Jingjing Gao[2,8], Li Cheng[3,8], Kunliang Bu[1], Zongxiu Wu[1], Ying Fei[1], Yuan Zheng[1], Li Wang[4], Fangsen Li[4], Xuan Luo[2], Zheng Liu[5]✉, Yuping Sun[2,6,7]✉ and Yi Yin[1,7]✉

The electronic evolution of doped Mott insulators has been extensively studied for decades in search of exotic physical phases. The proposed Mott insulator 1*T*-TaS_2 provides an intriguing platform to study the electronic evolution via doping. Here we apply scanning tunneling microscopy (STM) to study the evolution in Ti-doped 1*T*-TaS_2 at different doping levels. The doping Ti atom locally perturbs the electronic and spin state inside the doped star of David and induces a clover-shaped orbital texture at low-doping levels ($x < 0.01$). The insulator to metal transition occurs around a critical point $x = 0.01$, in which small metallic and large insulating domains coexist. The clover-shaped orbital texture emerges at a broader energy range, revealing a competition with the electron correlation. It transforms to a disorder-induced Anderson insulating behavior as doping increases. We directly visualize the trapped electrons in *dI*/*dV* conductance maps. The comprehensive study of the series of Ti-doped 1*T*-TaS_2 deepens our understanding of the electronic state evolution in a doped strong-correlated system.

npj Quantum Materials (2022)7:8 ; https://doi.org/10.1038/s41535-021-00415-5

INTRODUCTION

The strong electron–electron correlation in Mott insulators is a breeding ground for the emergence of exotic electronic states, most notably in the cuprate high T_c superconductors (HTS)[1,2]. Elemental doping can effectively tune a Mott insulator into other electronic phases like a metal, superconductor, etc.[3]. Understanding the evolution from a Mott insulator to a metallic phase, further to a superconducting state has been a central problem in the HTS studies[1–3]. Meanwhile, exotic quantum orders like checkerboard charge order, nematic order, etc. emerge during the doping evolution[4,5]. Another intriguing research field is discovering other types of Mott-insulating systems and then studying their exotic electronic states via different tuning methods[6,7]. The quasi-two-dimensional (2D) transition metal dichalcogenides 1*T*-TaS_2 is such a proposed Mott insulator[8–10].

The bulk 1*T*-TaS_2 exhibits an abundant phase diagram, which originates in the Mott insulating ground state in the commensurate charge-density-wave (CCDW) phase[11–14]. The coexistence or competition of electron–electron correlation and electron–phonon interaction has been intensively studied in 1*T*-TaS_2[14–16]. The insulating state resides on the quasi-2D triangular CCDW super-lattice instead of the atomic lattice. Each element of the super-lattice is called a star of David (SD), including a cluster of 13 Ta atoms (Fig. 1a). The multi-folding of SD super-lattice induces a narrow flat band near the Fermi level, which is half-filled with each SD contributing one unpaired orphan electron. A relatively strong correlation then leads to the split Hubbard bands and the Mott insulating gap[10]. Compared with traditional Mott insulators, the super-lattice and Mott insulating state in 1*T*-TaS_2 are very sensitive to external perturbations, providing complex phenomena for strong-correlation studies. The triangular super-lattice with a geometric frustration also enhances the quantum fluctuation, leading to a possible quantum spin liquid (QSL) state[17–19]. Recently, there are revived interests in the insulating nature of 1*T*-TaS_2, which may undermine the strong-correlation foundation[20–22]. Though numerous experiments have been performed on pristine samples, the origin of the insulating gap remains unclear[23–26]. The electronic evolution under different tuning methods provides alternative ways to reveal the nature of the insulating gap.

Scanning tunneling microscopy (STM) is a powerful technique to study the electronic evolution of doped Mott insulators at the atomic level. STM can locate the impurity dopants and investigate how a single dopant disturbs the local electronic density of state (DOS)[27,28]. In electronic spatial maps, STM can visualize the doping-dependent evolution of global DOS and the emergence of electronic orders[29,30]. Especially for 1*T*-TaS_2, nanostructures always appear in the bulk material[31–35], and STM is a valuable tool to explore the local electronic state before claiming macroscopic properties.

In this paper, we successfully synthesize the Ti-doped 1*T*-TaS_2 at a wide range of doping levels. The Ti doping replaces one of the 13 Ta^{4+} ([Xe]$4f^{14}$ $5d^1$) ions with a nonmagnetic and isovalent Ti^{4+} ([Ar]) ion, depleting the unpaired *d* electron in a SD. We combine STM and density functional theory (DFT) calculation to investigate how the electronic state is locally and globally disturbed. At a low-doping level $x < 0.01$, Ti atom locally perturbs the DOS inside SD, while an insulating state remains in undoped SDs. A Ti dopant effectively creates a spin vacancy in doped SD and possibly perturbs the QSL state[17–19] regardless of the substitution site. At the same time, the light doping induces a global clover-shaped orbital texture in *dI*/*dV* conductance maps. As the doping level increase to $x = 0.01$, the CCDW phase is completely suppressed,

[1]Zhejiang Province Key Laboratory of Quantum Technology and Device, Department of Physics, Zhejiang University, Hangzhou 310027, China. [2]Key Laboratory of Materials Physics, Institute of Solid State Physics, HFIPS Chinese Academy of Sciences, Hefei 230031, China. [3]Shenzhen Geim Graphene Center, Tsinghua-Berkeley Shenzhen Institute and Tsinghua Shenzhen International Graduate School, Tsinghua University, Shenzhen 518055, China. [4]Vacuum Interconnected Nanotech Workstation (Nano-X), Suzhou Institute of Nano-Tech and Nano-Bionics (SINANO), Chinese Academy of Sciences (CAS), Suzhou 215123, China. [5]Institute for Advanced Study, Tsinghua University, 100084 Beijing, China. [6]High Magnetic Field Laboratory, HFIPS Chinese Academy of Sciences, Hefei 230031, China. [7]Collaborative Innovation Center of Advanced Microstructures, Nanjing University, Nanjing 210093, China. [8]These authors contributed equally: Wenhao Zhang, Jingjing Gao, Li Cheng. ✉email: zheng-liu@tsinghua.edu.cn; ypsun@issp.ac.cn; yiyin@zju.edu.cn

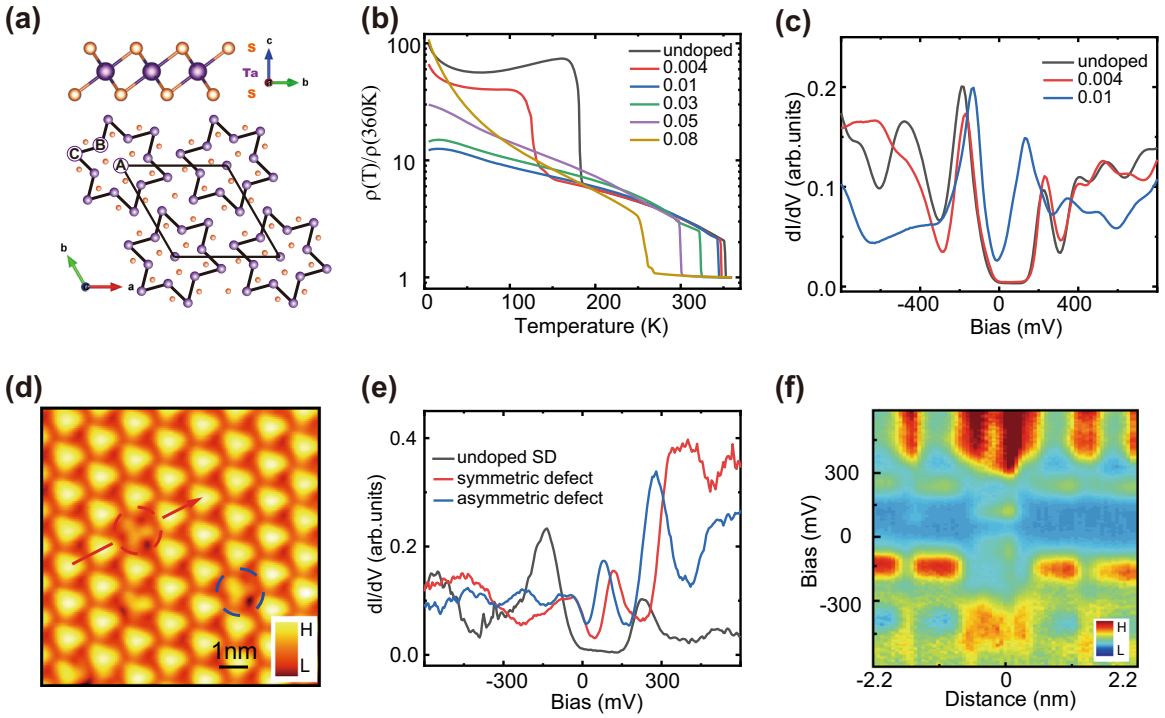

Fig. 1 Crystal structure and electronic state of 1*T*-($Ta_{1-x}Ti_x$)S_2. a Side- and top-view sketches present the crystal structure of single-layer 1*T*-TaS_2. Top-view sketch especially shows the cluster of SD and the $\sqrt{13}\times\sqrt{13}$ super-lattice. **b** Temperature-dependent in-plane resistivity ratio $\rho(T)/\rho(360K)$ for samples with different doping levels. **c** Typical *dI*/*dV* spectra of undoped, $x = 0.004$, and $x = 0.01$ samples. **d** A 9×9 nm^2 topography for the $x = 0.004$ sample ($V_b = -600$ mV, $I_s = 500$ pA). Red and blue circles mark a symmetric and an asymmetric Ti-doped SD, respectively. **e** The *dI*/*dV* spectra measured at the center of an undoped SD, a symmetric, and an asymmetric Ti-doped SDs, respectively. **f** A series of *dI*/*dV* spectra across the symmetric Ti-doped SD, along the red curve labeled in **d**.

and the low-temperature phase appears as a metallic state. The large and small domains coexist in the STM topography. In the large domain, the DOS of undoped SDs remains insulating as those in pristine samples. While in the small domain, the DOS exhibits a V-shaped metallic behavior near the Fermi level. The small metallic domains act as conducting channels, accompanied by the metallic domain walls. The CDW orbital texture in the metallic domain also expands to a wider energy range with increasing doping, competitive with the weakened correlation. When the doping level reaches 0.08, most SDs are doped by Ti atoms, and those undoped SD are randomly distributed in the topography. The analysis of conductance maps demonstrates that the unpaired electrons are trapped in undoped SDs. The low-temperature upturn of resistivity is related to the disorder-induced potential fluctuation, showing a typical Anderson insulator behavior.

RESULTS

Perturbation of Ti doping on the ground insulating state

We substitute Ti for Ta atoms to produce 1*T*-($Ta_{1-x}Ti_x$)S_2, with high-quality single-crystal samples grown by chemical vapor transport method. The similar ionic radii of Ti and Ta make the doping system relatively stable, and the doping has been precisely controlled during sample growth. With the Mott state in 1*T*-TaS_2 originating from the super-lattice of Ta atoms, a small amount of substitution of Ti for Ta can destroy the Mott insulating state. Figure 1b displays the temperature-dependent resistivity of 1*T*-($Ta_{1-x}Ti_x$)S_2. For the pristine sample, two clear phase transitions occur within the temperature range[11–13]. The transition around 350 K ($T_{I\text{-}NC}$) is associated with the incommensurate to nearly commensurate (NC) CDW transition. Below 175 K ($T_{NC\text{-}C}$), the material enters the CCDW phase. The NC-CCDW transition is sensitive to Ti doping. At $x = 0.004$, $T_{NC\text{-}C}$ decreases by about 50 K. From $x = 0.01$ and on, the transition completely disappears.

To infer the perturbation of 1*T*-TaS_2 by Ti doping, we first compare the extremely low-doped $x = 0.004$ sample with an undoped sample. For the undoped sample, STM topography shows a triangular SD super-lattice[16,31]. A typical *dI*/*dV* spectrum measured at the center of one SD is displayed in Fig. 1c. The sharp peaks at −190 and 220 meV correspond to the LHB and UHB, respectively. In our previous stacking-order-effect study[32], we have concluded that this spectrum mainly describes the Mott insulating property of the top single-layer 1*T*-TaS_2. For the $x = 0.004$ sample, the topography maintains a similar triangular SD super-lattice to the undoped one, with each SD appearing as a bright triangle (Fig. 1d). In Fig. 1c, a typical *dI*/*dV* spectrum of $x = 0.004$ sample also largely preserves the nature of the insulating state.

The scattered defective SDs can be identified under a negative bias voltage V_b, while difficult to discern under a positive bias voltage. As shown in Fig. 1d, a defective SD exhibits a clover shape with three petals. The defective SD within the red circle retains the three-fold rotational symmetry, while the one within the blue circle is asymmetric. Figure 1e presents the *dI*/*dV* spectra measured at the center of these two defective SDs. Compared with the spectrum of undoped SD, the most important changes are a suppression of the LHB (together with the insulating gap); and a transfer of the spectral weight from negative bias to positive bias. For both spectra, some in-gap state exists around the Fermi level, further discussed in the Supplementary Material (Supplementary Note 1). The difference between the two spectra is that the increased DOS at positive bias appears as a plateau for the symmetric defect and a peak for the asymmetric defect. In Fig. 1f, the linecut map suggests that Ti-induced perturbation is localized

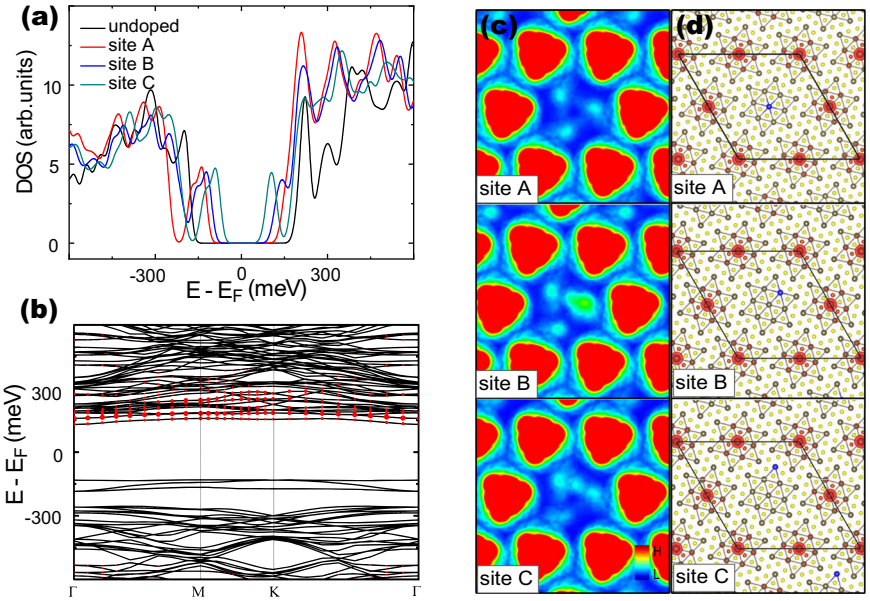

Fig. 2 First-principles DFT calculation of Ti-doped SD. a *dI/dV* spectrum, **b** band structure, **c** charge density, and **d** spin density for a 4-SD supercell. The three inequivalent substitution sites are marked by the blue atoms in **d**. **b** The band structure for the case where the central Ta is substituted by Ti. The three inequivalent substitution sites are marked by the blue atoms in **d**. Red contours in **c** and **d** represent high charge and spin densities, respectively.

inside the doped SD. All neighboring SDs maintain the Mott insulating state.

According to our first-principles simulation, the two types of defect patterns can be well reproduced by selecting the central (site A) or peripheral Ta (site B or C) as the Ti substitution sites (Fig. 2c). Two inequivalent peripheral sites (B or C) result in a similar asymmetric pattern with similar doping energy. The case of multiple Ti dopants within one SD is calculated to be energetically unfavored, and is thus not considered for low-doped samples. We further benchmark the defect *dI/dV* spectrum with first-principles DOS. The DFT calculation with +U correction (DFT + U) on a 1*T*-TaS_2 single layer provides a good description of the pristine insulating spectrum (Fig. 2a). Extending this calculation to a supercell containing a Ti-doped SD, we can also reproduce the overall spectrum profile and in particular the spectral weight transfer (Fig. 2a). Constraint by the computational sources available, the calculation is performed with respect to a $2\sqrt{13}\times 2\sqrt{13}$ supercell containing 4 SDs (51 Ta + 1 Ti + 104 S). By inspecting the orbital components, the strongly enhanced spectral peak around 300 meV is confirmed to be the empty *d*-orbitals of Ti atoms (Fig. 2b).

The spectral weight transfer has a direct impact on the spin state. While both Ta and Ti have the stable +4 valence state, Ta^{4+} is spin half, and Ti^{4+} is spin-zero. One occupied state associated with Ta is converted into an unoccupied state associated with Ti. With the LHB originally carrying the spin degree of freedom, the suppression of the LHB is evident in the defect spectrum. The doped SD loses the vital orphan electron, leaving no room for spin degeneracy, and Ti doping effectively tunes a SD into a spin vacancy. Regardless of the substitution site, the DFT + U spin density plot (Fig. 2d) explicitly shows the absence of local moment at defective SDs. The spin state of 1*T*-TaS_2 is intricate due to strong geometry fluctuation and possible QSL state[17,18]. In the QSL state, the spin vacancy possibly liberates a free moment in neighboring SDs, which increases the local moment density[19]. We do not observe any signals of the liberated free moment with our local probe tool of STM. We perform magnetic susceptibility measurement in three low-doping samples (Supplementary Note 2). The local moment density slightly increases with the doping level. More experiments with other techniques are required to confirm this point[36–38].

We perform *dI/dV* mapping measurement around a Ti-doped SD at different energies to better understand the Ti doping effect. Figure 3 displays the comparison between *dI/dV* maps and DFT + U DOS maps at four characteristic energies. The upper row of Fig. 3a–d displays experimental *dI/dV* maps at energies (−380, −170, 360, 560) mV. The most important change at the defective SD is related to the map at −170 mV, the energy roughly coinciding with the LHB. The DOS almost vanishes on the Ti-doped SD, consistent with the suppressed LHB in the defect spectrum. Also reproduced in Fig. 3f, this map provides further evidence that Ti substitution converts the SD into a spinless site. The high intensity on Ti-doped SD in Fig. 2c, g is also consistent with the spectral weight transfer induced by the Ti doping.

In addition to the local effect of Ti doping, the most surprising result is that unusual orbital textures appear on both Ti-doped and undoped SDs (Fig. 3). In Fig. 3a, the three petals are more separated on Ti-doped SD comparing with those on undoped SDs. Due to LHB suppression at doped SD, the three-petal feature at −380 mV becomes prominent in the negative-voltage-biased topography. The three petal orbital textures have rarely appeared in the pristine sample of 1*T*-TaS_2[16], as shown in Supplementary Fig. 6. In Fig. 3c, d, other intricate orbital textures can also be observed. The map at 360 mV shows inverted triangular patterns. The map at 560 mV shows a network of triangles with strong intensity distributed on peripheral Ta atoms. Both featured patterns can be roughly reproduced in Fig. 3g, h. Most related with the CDW phase, the orbital textures are described in more detail (Supplementary Note 4). The dilute Ti doping locally impacts the DOS on the Ti-doped SD and globally induces clover-shaped orbital textures in the CDW phase.

Mott insulator to metal transition at low-doping level

We next focus on the $x = 0.01$ sample. The NCCDW-CCDW transition disappears in the resistivity measurement, showing a macroscopic metallic ground state. Figure 4a shows a 75×75 nm^2 topography of $x = 0.01$ sample, in which large (top-left and bottom-right areas) and small domains coexist. Ti-doped SDs are

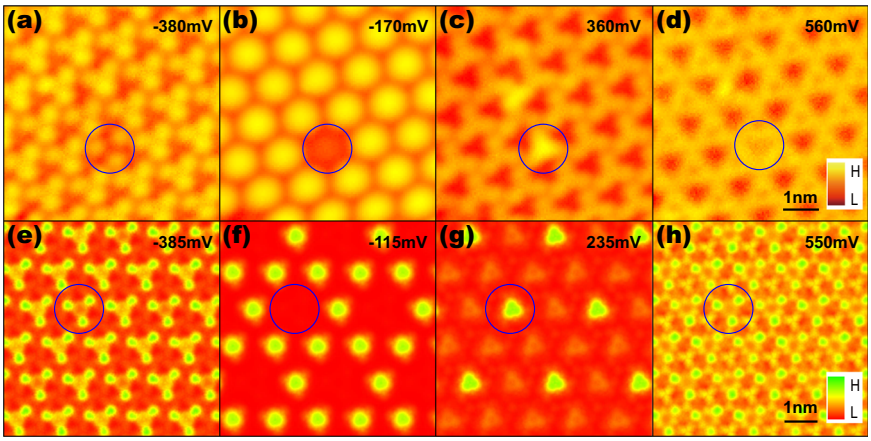

Fig. 3 Orbital textures around a symmetric Ti-doped SD at different energies. a–d Experimental *dI/dV* maps at −380, −170, 360, and 560 mV. The Ti-doped SD shows a dim (bright) intensity below (above) the Fermi level. The sample shows a three-fold symmetry in other three *dI/dV* maps. **e–h** First-principle partial charge within a 35 meV energy window centered at four characteristic energies. The small difference between experimental and theoretical energies are chosen to clearly present the prominent features.

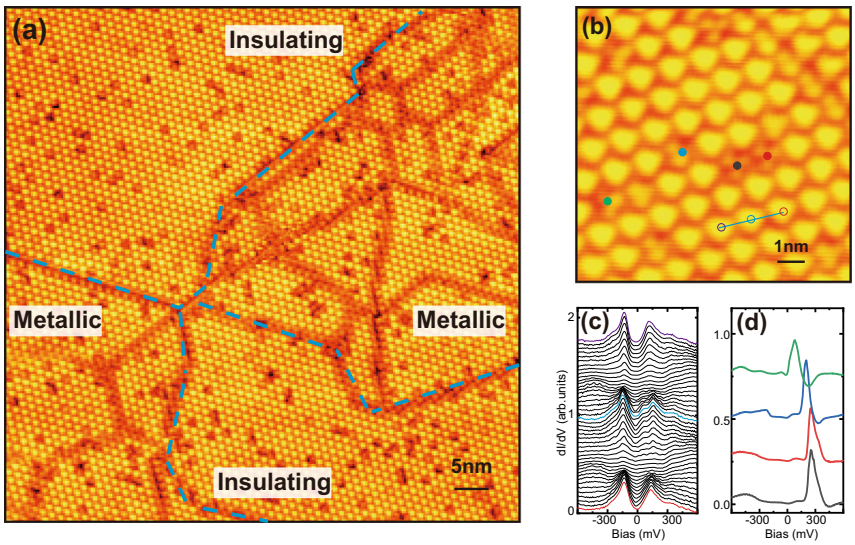

Fig. 4 Topography and electronic state for a $x = 0.01$ sample. a A 75×75 nm^2 topography ($V_b = -1$ V, $I_s = 100$ pA) shows the coexistence of insulating large domains and metallic small domains. **b** A 10×10 nm^2 topography insides a metallic domain. The gray, red, blue, and green circles mark four different Ti-doped SDs. **c** A series of *dI/dV* spectra measured along the blue line in **b**. **d** Four typical *dI/dV* spectra on symmetric and asymmetric Ti-doped SDs.

randomly scattered in the field of view (FOV). The domains are generally related to the doping-induced subtle modification of crystal structure and a destabilization of the $\sqrt{13} \times \sqrt{13}$ structure[16,33,39,40]. The multiple domain walls provide metallic and conductive transport channels in the NCCDW phase[34,35,41]. The insulating state is still preserved within large domains. The Ti doping effect in the large insulating domain is similar to that in the $x = 0.004$ sample.

Within small domains, the *dI/dV* spectrum appears as a V-shaped metallic one, as shown in Fig. 1c. Small metallic domains provide additional conductive channels besides the domain walls. In Fig. 4b, we show an 8×8 nm^2 topography of a metallic domain. A linecut of *dI/dV* spectrum is measured along the blue line crossing three undoped SDs, with results shown in the waterfall graph in Fig. 4c. Peaks of the V-shaped feature show a periodic variation, with the strongest intensity at the SD center. This low-energy feature around the Fermi level also shows competition with the CDW peaks at higher energy, with the strongest intensity shifted by half the period. Similar to that in pristine 1*T*-TaS_2, the low-energy bands originate from the central Ta orbital, and the CDW bands are from the surrounding Ta orbitals[16]. Besides, some variation exists in different V-shaped metallic spectra. For example, a low-energy in-gap state emerges in the blue spectrum in Fig. 4c. This kind of variation is ubiquitous in metallic domains. In the cuprate superconductor[27,29,30], the doping triggers a spectral weight transfer from Hubbard bands to low-energy states near the Fermi level, resulting in a V-shaped pseudogap upon doping. For 1*T*-$(Ta_{1-x}Ti_x)S_2$, we observe the appearance of V-shaped (pseudogap) spectra in small domains after Ti doping introduces holes and destroys the electron correlation. The domain wall *dI/dV* spectrum is also measured and shown in Supplementary Fig. 5, exhibiting a metallic behavior. The metallic transport behavior should be from both the metallic V-shaped spectra within domains and the metallic domain walls, with the former related to the Ti doping-induced insulator-to-metal transition that we are more interested. Compared with the NCCDW phase in undoped 1*T*-TaS_2[41], the low-temperature NCCDW phase of Ti-doped 1*T*-TaS_2 ($x = 0.01$) has some similarities. They all share nano-sized domains and metallic spectra. The detailed spectral differences in two NCCDW phases, however, can not be distinguished by macroscopic transport

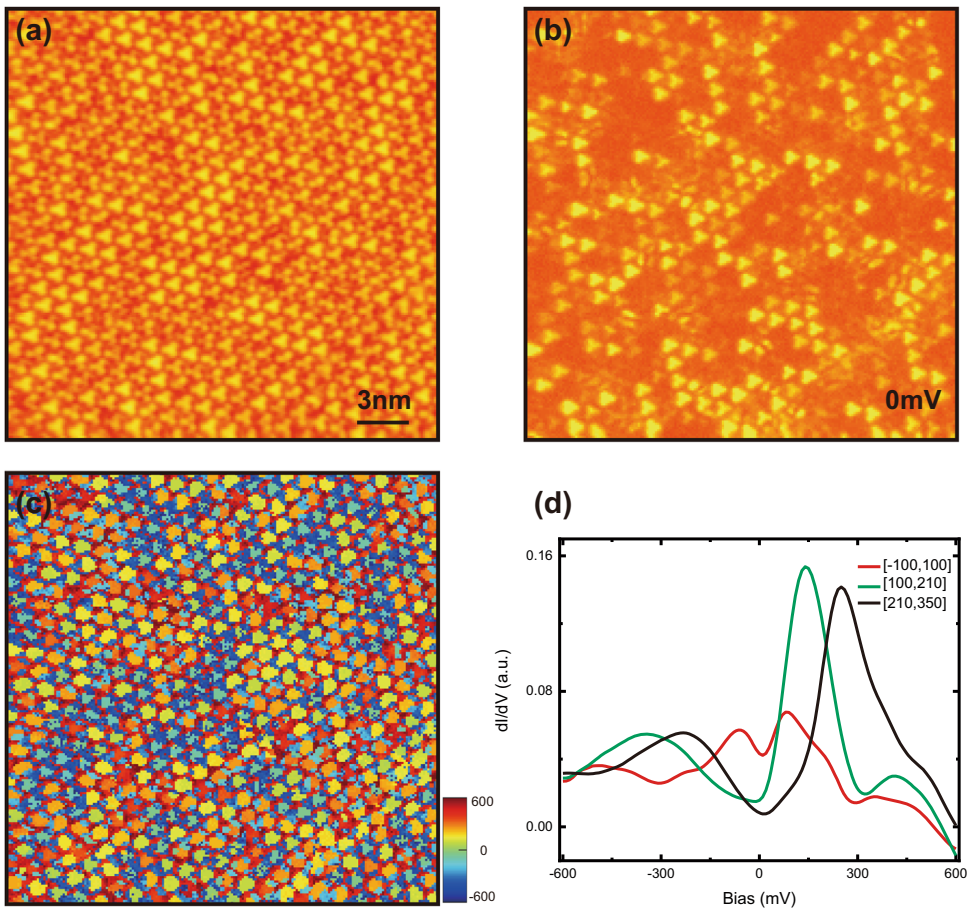

Fig. 5 Disorder at a $x = 0.08$ sample. a A $30 \times 30\ nm^2$ topography for a $x = 0.08$ sample ($V_b = -600$ mV, $I_s = 500$ pA). **b** The *dI/dV* map at the Fermi level. The high intensity area corresponds to the undoped SDs in topography. **c** The maximum peak map of the *dI/dV* spectra in the same area. **d** The averaged *dI/dV* spectra of different range in the maximum peak map.

measurement. By counting doped SD in both insulating and metallic domains, we think that the doping density does not determine whether the area is insulating or metallic. It is possible that some local material details randomly trigger the appearance of the domain wall network around the critical doping level, and the correlated state in small domains is more prone to be destabilized to a metallic state.

For the local Ti doping effect in metallic domains, Fig. 4d shows the *dI/dV* spectra measured at four Ti-doped SDs in Fig. 4b. The spectral features are different from that of doped SDs in the Mott insulating state. The Ti-induced plateau or peak are both changed to an enhanced peak above the Fermi level. The peak locates at variable energies for different doped SDs. For SD with Ti doping at the B/C site, the peak location in spectrum is relatively closer to the Fermi level. The anomalous enhanced peak at positive bias is still related to the *d*-orbitals of Ti atom. The in-gap state also exists around the Fermi level, although less apparent against the high peak.

The three-petal orbital texture still exists in *dI/dV* maps of the metallic domain, even in an energy range several times wider than that in $x = 0.004$ sample. For the $x = 0.004$ sample (Supplementary Fig. 7), the orbital texture starts to appear around the dip energy between the LHB and the negative-bias CDW peak. For the $x = 0.01$ sample (Supplementary Fig. 8), the insulating spectrum changes to a metallic spectrum in the metallic domain. It seems that the negative-bias CDW peak shifts to the lower energy. The energy range of the dip between the LHB and the negative-bias CDW peak is broader, corresponding to the broader range in which the orbital texture exists. The orbital texture with a three-petal feature may be related to a spatially redistributed spectral weight between the central Ta and neighboring Ta atoms. The Mott gap gradually collapses with increasing doping, and the orbital texture's energy range expands, reflecting the competition between electron correlation and the orbital texture structure. When the Ti doping weakens the electron correlation, this competing CDW orbital texture is gradually induced and enhanced. This global change starts to appear even earlier than the V-shaped pseudogap state. In the cuprate superconductor[29], a checkerboard charge order has emerged in the lightly doped sample. The orbital texture could be a similar emergent phenomenon, indicating a competition and delicate balance between the electron correlation and the orbital texture structure. Another orbital texture has been found to coexist with the Mott insulating state in the MBE-grown single-layer 1*T*-$TaSe_2$[42].

Metal to insulator transition at high doping level

Doping inevitably brings disorder to the system. As the doping amount increases from 0.01 to 0.05, the low-temperature resistivity keeps decreasing (Fig. 1b). However, when the doping rises to 0.08, the low-temperature resistivity shows an upward trend. This reentrance of insulating behavior indicates a competition possibly from the disorder effect under high doping. For the $x = 0.08$ sample, Fig. 5a displays a $30 \times 30\ nm^2$ topography taken under a bias voltage $V_b = -600$ mV. Ideally, the nominal doping level $x = 0.08$ corresponds to the doping of one Ti atom per SD. In the negative-voltage-biased topography (Fig. 5a), the three petal-shaped SDs are ubiquitous, together with some bright undoped

SDs scattered in the FOV. The Ti-doped SDs are either symmetric or asymmetric three-petal-shaped. The random sites of Ti doping in SDs result in a periodic potential with disorder-induced fluctuations.

For a detailed analysis of the electronic state, we perform the *dI*/*dV* spectrum measurement on a 200×200 grid in this FOV. As shown in Fig. 5b, the zero-bias *dI*/*dV* map exhibits a strong spatial fluctuation. The bright triangles with high intensity have a one-to-one correspondence with undoped SDs in the topography. We further classify the spectra by seeking the voltage at which the highest peak is located in each spectrum and map the spatial-dependent peak voltage. In Fig. 5c, the map of peak voltage shows a random distribution at different SDs but is relatively homogeneous within each SD, which is consistent with that each SD is considered as a super-lattice site in the framework of Mott physics for 1*T*-TaS_2.

Guided by the distribution of peak voltage, we calculate the average *dI*/*dV* spectra whose peak voltage is within a certain range. Figure 5d shows three representative averaged *dI*/*dV* spectra whose peak voltages are within [−100, 100] mV, [100, 210] mV, and [210, 350] mV. For the average spectrum with peak voltage around the Fermi level ([−100, 100] mV), the zero-bias conductance is enhanced, together with a V-shaped feature and two peaks. The spatial distribution (green-yellow spots in Fig. 5c) of these spectra is mainly consistent with the undoped SD positions. The collected information implies that this average spectrum is characteristic of undoped SDs. For the average *dI*/*dV* spectra in the range of [100, 210] mV and [210, 350] mV, a strongly enhanced peak exists around 150 and 250 mV, respectively. We attribute the peaks to Ti-induced band features for spectra on doped SDs. For the average spectra with a negative peak voltage, we find in Fig. 5c that some of them correspond to the dark blue spots between SDs. Similar to the periodic variation of pseudogap peaks and CDW peaks, the negative CDW peak can increase to the maximum at spatial positions between SDs.

The $x = 0.08$ sample has been turned much away from half-filling. For remaining undoped SDs, the central Ta atom contributes an unpaired electron. The DOS of undoped SD maintains the V-shape and two peak features, similar to the V-shaped metallic spectrum in the $x = 0.01$ sample. The disorder-induced potential fluctuation is likely to be the dominant factor to cause such a consequence. The orphan electrons are trapped and localized at undoped SDs, resulting in an Anderson insulator at this high doping level.

Discussion

The ground state of 1*T*-TaS_2 is intriguing and puzzling because of the coexistence and competition of different kinds of interactions. The origin of the insulating state of 1*T*-TaS_2 is still debatable. Recent first-principles calculations and several experiments suggest that a double-layer stacking order leads to a band-gap insulator instead of a Mott insulator[20–26]. The role of stacking order has been studied in detail in our previous work[32]. In 1*T*-$(Ta_{1-x}Ti_x)S_2$, the absence of local free moment at doped SD is also slightly against the double-layer band insulator scenario. The large insulating gap is still a correlation-induced Mott insulating gap, the property of the top single-layer 1*T*-TaS_2. The possible stacking-order-effect in mosaic domains is also not observed. One intuition is that Ti doping is a strong perturbation within each layer of 1*T*-TaS_2 and satisfies the doped Hubbard model, which should also be a dominant effect compared with the interlayer stacking perturbation. This point may explain why researchers do not need to consider the stacking-order effect for different doped systems with multiple domains[16].

In the presence of a strong electron correlation, the triangular SD super-lattice is a possible QSL state due to geometry fluctuation. In the extremely low-doped system, each Ti atom removes one electron in the triangular super-lattice site and perturbs the ground state of 1*T*-TaS_2. The Ti doping modifies the local electronic state and alters the spin configuration to a spin vacancy[43]. The spin vacancy possibly liberates a free moment in neighboring sites, and other experimental techniques are required to detect such microscopic spin-channel signals.

When doped away from the half-filling, the Mott insulator generally evolves to a metallic, especially a pseudogap state. With the Mott state residing on the CCDW super-lattice, the insulator to metal transition in 1*T*-$(Ta_{1-x}Ti_x)S_2$ starts to appear within small metallic domains, at a critical doping $x = 0.01$. As the doping level increases to $x = 0.08$, most SDs include doped Ti atoms and the disorder plays a vital role in the system. The spectrum peak distribution reveals the potential fluctuation, which is crucial to trap and localize unpaired electrons. The reentrance of low-temperature insulator behavior is compatible with the Anderson insulator phenomenon.

Exotic orders emerge in the electronic evolution of the doped Mott system. For example, the checkerboard charge order appears in the lightly doped cuprate superconductor[29]. The competition between near-degenerate ground states is prominent in the theoretical calculation of the doped Hubbard model[44–46]. In 1*T*-$(Ta_{1-x}Ti_x)S_2$, a clover-shaped orbital texture starts to appear in the low-doping-level sample and exists within a broader energy range as the doping increases. The energy-dependent charge order in STM *dI*/*dV* maps relates the charge order with corresponding electronic bands. The energy-dependent orbital texture reveals both the charge-order-band relation and the orbital distribution pattern of such order. Our results present the competition between the much complex charge order behavior and the electronic correlation.

In summary, we performed detailed STM measurements to study the electronic evolution of 1*T*-$(Ta_{1-x}Ti_x)S_2$ at a wide range of doping level. The precise dopant positioning enables the detection of Ti-induced local disturbance. Combining with the first-principles calculation, we demonstrate a slight Ti doping ($x < 0.01$) locally modifies the DOS of doped SD and creates a spin vacancy on site. When the doping $x > 0.01$, small metallic domains and domain walls lead to the insulator-metal transition. In the evolution process, some orbital textures emerge globally and compete with the suppressed electronic correlation. As the doping increases, the disorder drives the system to an Anderson insulator. The comprehensive study of 1*T*-$(Ta_{1-x}Ti_x)S_2$ deepens our understanding of the strongly correlated physics and deserves more theoretical exploration.

METHODS

Sample preparation

The high-quality 1*T*-$(Ta_{1-x}Ti_x)S_2$ single-crystal samples were grown by the chemical vapor transport (CVT) method with iodine as the transport agent. Ta (99.99%, Aladdin), Ti (99.99%, Aladdin), and S (99.99%, Aladdin) powders with a nominal mole ratio of $1 - x$:x:2 were weighted, mixed with 0.2 g of I_2, and placed into silicon quartz tubes. The quartz tubes were sealed under high vacuum and heated in the two-zone furnace for 10 days, in which the temperature of source and growth zones were fixed at 900 and 800 °C. Then the tubes were removed and quenched in an ice water mixture, after which single crystals were collected for measurements. The doping has been uniformly and precisely controlled in high-quality samples. The average stoichiometry was determined by examination of multiple points using X-ray energy dispersive spectroscopy (EDS). Since the minimum resolution of EDS is about 0.01 for Ti content, the doping content smaller than 0.01 is calibrated by the relative phase transition temperatures.

STM measurements

The STM measurements were performed in two different commercial STM systems showing no obvious difference. The samples were gradually cooled to around 80 K, in situ cleaved and transferred to the STM head for an immediate measurement. Electrochemically etched tungsten tips were

used after calibration on single crystalline with an Au (111) surface. Data were collected at either 4.5 K or 77 K, both of which are far below the transition temperature. Other than a small thermal broadening, the data taken at 77 K is very similar to that taken at 4.5 K, and does not affect the physics we discussed in this work. The *dI/dV* spectra were taken in a standard lock-in technique with a frequency of 1213.7 Hz and an amplitude of 10 mV[31].

First-principles calculation

The first-principles calculations were performed using the Vienna ab initio Simulation Package[47–50], with the projector augmented wave method[51] and the Perdew-Burke-Ernzerhof exchange-correlation functional[52]. The +U correction was employed to capture the Coulomb interaction of Ta 5*d* orbitals on the Hartree-Fock level, following the simplified (rotational invariant) approach introduced by Dudarev[53]. We applied an effective $U = 2.27$ eV as previously derived from the linear-response calculation[54]. All our simulation cells contain a single layer of 4 SDs and with a 15 Å vacuum to prevent interlayer coupling between different layers. The plane-wave cutoff was set to 300 eV. For integration over the Brillouin zone, a Γ-centered $3 \times 3 \times 1$ k-point mesh for the computation of the structure relaxations and the self-consistent electronic densities, and a denser, $7 \times 7 \times 1$ mesh for the computation of the densities of states. Convergence is reached if the consecutive energy difference is within 10^{-5} eV for electronic iterations and the forces are less than 0.002 eV Å^{-1}. We relaxed the structures after substituting Ti for Ta. Substitution of the central Ta site (site1) is found to have the lowest energy. The substitution energies of the two peripheral Ta sites are 193 meV per Ti (site 2) and 178 meV per Ti (site 3) higher.

DATA AVAILABILITY

The source data and related supporting information are available from the corresponding author upon request.

Received: 5 September 2021; Accepted: 10 December 2021;
Published online: 17 January 2022

REFERENCES

1. Keimer, B., Kivelson, S. A., Norman, M. R. & Zaanen, J. From quantum matter to high-temperature superconductivity in copper oxides. *Nature* **518**, 179–186 (2015).
2. Dagotto, E. Complexity in strongly correlated electronic systems. *Science* **309**, 257–262 (2005).
3. Lee, P. A., Nagaosa, N. & Wen, X. G. Doping a Mott insulator: physics of high-temperature superconductivity. *Rev. Mod. Phys.* **78**, 17 (2006).
4. Hoffman, J. E. et al. A Four unit cell periodic pattern of quasi-particle states surrounding vortex cores in $Bi_2Sr_2CaCu_2O_{8+\delta}$. *Science* **295**, 466–469 (2002).
5. Sprau, P. O. et al. Discovery of orbital-selective Cooper pairing in FeSe. *Science* **357**, 75–80 (2017).
6. Cao, Y. et al. Unconventional superconductivity in magic-angle graphene superlattices. *Nature* **556**, 43–50 (2018).
7. Regan, E. C. et al. Mott and generalized Wigner crystal states in WSe_2/WS_2 moire superlattices. *Nature* **579**, 359–363 (2020).
8. Smith, N. V., Kevan, S. D. & Di Salvo, F. J. Band structures of the layer compounds 1*T*-TaS_2 and 2*H*-$TaSe_2$ in the presence of commensurate charge-density waves. *J. Phys. C: Solid State Phys.* **18**, 3175 (1985).
9. Rossnagel, K. & Smith, N. V. Spin-orbit coupling in the band structure of reconstructed 1*T*-TaS_2. *Phys. Rev. B* **73**, 073106 (2006).
10. Kim, J. J., Yamaguchi, W., Hasegawa, T. & Kitazawa, K. Observation of Mott localization gap using low temperature scanning tunneling spectroscopy in commensurate 1*T*-TaS_2. *Phys. Rev. Lett.* **73**, 2103 (1994).
11. Wilson, J. A., Di Salvo, F. J. & Mahajan, S. Charge-density waves and superlattices in the metallic layered transition metal dichalcogenides. *Adv. Phys.* **24**, 117–201 (1975).
12. Di Salvo, F. J., Wilson, J. A., Bagley, B. G. & Waszczak, J. V. Effects of doping on charge-density waves in layer compounds. *Phys. Rev. B* **12**, 2220–2235 (1975).
13. Fazekas, P. & Tosatti, E. Electrical, structural and magnetic properties of pure and doped 1*T*-TaS_2. *Philos. Mag. B* **39**, 229–244 (1979).
14. Sipos, B. et al. From Mott state to superconductivity in 1*T*-TaS_2. *Nat. Mater.* **7**, 960–965 (2008).
15. Cho, D. et al. Interplay of electron-electron and electron-phonon interactions in the low-temperature phase of 1*T*-TaS_2. *Phys. Rev. B* **92**, 085132 (2015).
16. Qiao, S. et al. Mottness collapse in 1*T*-$TaS_{2-x}Se_x$ transition-metal dichalcogenide: an interplay between localized and itinerant orbitals. *Phys. Rev. X* **7**, 041054 (2017).
17. Law, K. T. & Lee, P. A. 1*T*-TaS_2 as a quantum spin liquid. *Proc. Natl. Acad. Sci. USA* **114**, 6996–7000 (2017).
18. He, W. Y. et al. Spinon Fermi surface in a cluster Mott insulator model on a triangular lattice and possible application to 1*T*-TaS_2. *Phys. Rev. Lett.* **121**, 046401 (2018).
19. Anderson, P. W. The resonating valence bond state in La_2CuO_4 and superconductivity. *Science* **235**, 1196–1198 (1987).
20. Ritschel, T. et al. Orbital textures and charge density waves in transition metal dichalcogenides. *Nat. Phys.* **11**, 328–331 (2015).
21. Ritschel, T., Berger, H. & Geck, J. Stacking-driven gap formation in layered 1*T*-TaS_2. *Phys. Rev. B* **98**, 195134 (2018).
22. Lee, S. H., Goh, J. S. & Cho, D. Origin of the insulating phase and first-order metal-insulator transition in 1*T*-TaS_2. *Phys. Rev. Lett.* **122**, 106404 (2019).
23. Butler, C. J., Yoshida, M., Hanaguri, T. & Iwasa, Y. Mottness versus unit-cell doubling as the driver of the insulating state in 1*T*-TaS_2. *Nat. Commun.* **11**, 2477 (2020).
24. Butler, C. J., Yoshida, M., Hanaguri, T. & Iwasa, Y. Doublonlike excitations and their phononic coupling in a Mott charge-density-wave system. *Phys. Rev. X* **11**, 011059 (2021).
25. Lee, J., Jin, K. H. & Yeom, H. W. Distinguishing a Mott insulator from a trivial insulator with atomic adsorbates. *Phys. Rev. Lett.* **126**, 196405 (2021).
26. Wang, Y. D. et al. Band insulator to Mott insulator transition in 1*T*-TaS_2. *Nat. Commun.* **11**, 4215 (2020).
27. Ye, C. et al. Visualizing the atomic scale electronic structure of the $Ca_2CuO_2Cl_2$ Mott insulator. *Nat. Commun.* **4**, 1365 (2013).
28. Pan, S. H. et al. Imaging the effects of individual zinc impurity atoms on superconductivity in $Bi_2Sr_2CaCu_2O_{8+\delta}$. *Nature* **403**, 746–750 (2000).
29. Cai, P. et al. Visualizing the evolution from the Mott insulator to a charge-ordered insulator in lightly doped cuprates. *Nat. Phys.* **12**, 1047–1051 (2016).
30. Kohsaka, Y. et al. Visualization of the emergence of the pseudogap state and the evolution to superconductivity in a lightly hole-doped Mott insulator. *Nat. Phys.* **8**, 534–538 (2012).
31. Bu, K. L. et al. Possible strain induced Mott gap collapse in 1*T*-TaS_2. *Commun. Phys.* **2**, 146 (2019).
32. Wu, Z. X. et al. Effect of stacking order on the electronic state of 1*T*-TaS_2. *Phys. Rev. B*, Preprint at https://arxiv.org/abs/2105.08663 (2021).
33. Ohta, S. et al. Evolution of electronic states during change from a Mott commensurate to a nearly commensurate state in Nb-substituted 1*T*-TaS_2 observed by scanning tunneling microscopy and spectroscopy. *Phys. Rev. B* **103**, 155137 (2021).
34. Gerasimenko, Y. A. et al. Intertwined chiral charge orders and topological stabilization of the light-induced state of a prototypical transition metal dichalcogenide. *npj Quantum. Mater.* **4**, 32 (2019).
35. Cho, D. et al. Correlated electronic states at domain walls of a Mott-charge-density-wave insulator 1*T*-TaS_2. *Nat. Commun.* **8**, 392 (2017).
36. Klanjšek, M. et al. A high-temperature quantum spin liquid with polaron spins. *Nat. Phys.* **13**, 1130–1134 (2017).
37. Kratochvilova, M. et al. The low-temperature highly correlated quantum phase in the charge-density-wave 1*T*-TaS_2 compound. *npj Quantum. Mater.* **2**, 42 (2017).
38. Murayama, H. et al. Effect of quenched disorder on the quantum spin liquid state of the triangular-lattice antiferromagnet 1*T*-TaS_2. *Phys. Rev. Res.* **2**, 013099 (2020).
39. Li, L. J. et al. Fe-doping-induced superconductivity in the charge-density-wave system 1*T*-TaS_2. *Europhys. Lett.* **97**, 67005 (2012).
40. Fujisawa, Y. et al. Appearance of a domain structure and its electronic states in iron doped 1*T*-TaS_2 observed using scanning tunneling microscopy and spectroscopy. *J. Phys. Soc. Jpn.* **86**, 113703 (2017).
41. Lutsyk, I. et al. Electronic structure of commensurate, nearly commensurate, and incommensurate phases of 1*T*-TaS_2 by angle-resolved photoelectron spectroscopy, scanning tunneling spectroscopy, and density functional theory. *Phys. Rev. B* **98**, 195425 (2018).
42. Chen, Y. et al. Strong correlations and orbital texture in single-layer 1*T*-$TaSe_2$. *Nat. Phys.* **16**, 218–224 (2020).
43. Julien, M. H. et al. ^{63}Cu NMR evidence for enhanced antiferromagnetic correlations around Zn impurities in $YBa_2Cu_3O_{6.7}$. *Phys. Rev. Lett.* **84**, 3422–3425 (2000).
44. Zheng, B. X. et al. Stripe order in the underdoped region of the two-dimensional Hubbard model. *Science* **358**, 1155–1160 (2017).
45. Huang, E. W. et al. Numerical evidence of fluctuating stripes in the normal state of high-T_c cuprate superconductors. *Science* **358**, 1161–1164 (2017).
46. Jiang, H. C. & Devereaux, T. P. Superconductivity in the doped Hubbard model and its interplay with next-nearest hopping *t*.′ *Science* **365**, 1424–1428 (2019).
47. Kresse, G. & Hafner, J. Ab initio molecular dynamics for liquid metals. *Phys. Rev. B* **47**, 558–561 (1993).

48. Kresse, G. & Hafner, J. Ab initio molecular-dynamics simulation of the liquid-metal-amorphous-semiconductor transition in germanium. *Phys. Rev. B* **49**, 14251–14269 (1994).
49. Kresse, G. & Furthmüller, J. Efficiency of ab-initio total energy calculations for metals and semiconductors using a plane-wave basis set. *Comp. Mater. Sci.* **6**, 15–50 (1996).
50. Kresse, G. & Furthmüller, J. Efficient iterative schemes for ab initio total-energy calculations using a plane-wave basis set. *Phys. Rev. B* **54**, 11169 (1996).
51. Kresse, G. & Joubert, D. From ultrasoft pseudopotentials to the projector augmented-wave method. *Phys. Rev. B* **59**, 1758–1775 (1999).
52. Perdew, J. P., Burke, K. & Ernzerhof, M. Generalized gradient approximation made simple. *Phys. Rev. Lett.* **77**, 3865–3868 (1996).
53. Dudarev, S. L. et al. Electron-energy-loss spectra and the structural stability of nickel oxide: An LSDA+ U study. *Phys. Rev. B* **57**, 1505–1509 (1998).
54. Darancet, P., Millis, A. J. & Marianetti, C. A. Three-dimensional metallic and two-dimensional insulating behavior in octahedral tantalum dichalcogenides. *Phys. Rev. B* **90**, 045134 (2014).

ACKNOWLEDGEMENTS

This work was supported by the National Key Research and Development Program (2019YFA0308602), the Key Research and Development Program of Zhejiang Province, China (2021C01002), Vacuum Interconnected Nanotech Workstation (Nano-X) (No: B2004) and the Fundamental Research Funds for the Central Universities in China. Z.L. thanks the National Nature Science Foundation of China (NSFC-11774196) and Tsinghua University Initiative Scientific Research Program. J.G., X.L., and Y.S. thank the support of the National Key Research and Development Program (2016YFA0300404), the National Natural Science Foundation of China (NSFC-11674326, NSFC-11874357), the Joint Funds of the National Natural Science Foundation of China, and the Chinese Academy of Sciences' Large-Scale Scientific Facility (U1832141, U1932217, U2032215).

AUTHOR CONTRIBUTIONS

W.Z., J.G., and L.C. contributed equally to this work. W.Z., K.B., and Z.W. conducted the STM experiment. J.G., X.L., and Y.S. grew the samples and performed the resistivity and magnetic susceptibility measurement. L.C. and Z.L. performed the DFT calculation. Y.F., Y.Z., L.W., and F.L. discussed the experiment and results. W.Z., Y.Y., and Z.L. wrote the paper. Y.Y. supervised the experiments. All authors have read the paper and approved it.

COMPETING INTERESTS

The authors declare no competing interests.

ADDITIONAL INFORMATION

Supplementary information The online version contains supplementary material available at https://doi.org/10.1038/s41535-021-00415-5.

Correspondence and requests for materials should be addressed to Zheng Liu, Yuping Sun or Yi Yin.

Reprints and permission information is available at http://www.nature.com/reprints

Publisher's note Springer Nature remains neutral with regard to jurisdictional claims in published maps and institutional affiliations.